

Article

Historical aerial surveys map long-term changes of forest cover and structure in the central Congo Basin

Koen Hufkens^{1,2,*}, Thalès de Haulleville³, Elizabeth Kearsley¹, Kim Jacobsen^{1,3}, Hans Beeckman³, Piet Stoffelen⁴, Filip Vandelook⁴, Sofie Meeus⁴, Michael Amara⁵, Leen Van Hirtum⁵, Jan Van den Bulcke¹, Hans Verbeeck¹, Lisa Wingate²

¹ Ghent University, Ghent, Belgium;

² INRA, UMR ISPA, Villenave d'Ornon, France;

³ Royal Museum for Central Africa, Tervuren, Belgium;

⁴ Botanic Garden Meise, Meise, Belgium;

⁵ National Archives of Belgium, Brussels, Belgium;

* Correspondence: koen.hufkens@gmail.com

Version January 23, 2020 submitted to Remote Sens.



1 **Abstract:** Land Use and Land Cover change (LULCC) of African rainforest contribute to global carbon
2 emissions. Yet, most historical estimates of LULCC and their carbon emissions rely on non-spatially
3 explicitly data in the pre-satellite era (< 1972). Past studies have expanded this pre-satellite time
4 frame with declassified satellite surveillance data or aerial surveys, but none cover the Congo Basin.
5 Here, we use historical aerial survey photos to map the extent and structure of LULCC around
6 Yangambi, central Congo Basin, in 1958. Our study leveraged Structure-from-Motion to generate
7 a large orthomosaic covering 82800 ha, counting 733 million pixels, at a sub meter resolution and
8 geo-referenced to $\sim 4.7 \pm 4.3$ m. Primary forest in the orthomosaic was classified with a Convolutional
9 Neural Network Deep Learning approach. We used these data to quantify LULCC, landscape and
10 canopy complexity and scale above ground biomass between historical and contemporary condition.
11 We show a shift from historical highly structured industrial deforestation in 1958 (16200 ha), to
12 contemporary smallholder farming clearing (8800 ha), increasing landscape fragmentation and
13 forest edges. Efforts to quantify canopy texture and their link to carbon storage had limited to no
14 success. Our analysis provides an insight in key spatial and temporal patterns of deforestation and
15 reforestation at a multi-decadal scale and provide a historical context to land-cover and land-use
16 change spatial patterns for past and ongoing field research in the area.

17 **Keywords:** Aerial survey, data recovery, CNN, Deep Learning, SfM, Congo Basin

18 1. Introduction

19 Tropical ecosystem services are severely impacted by deforestation and forest degradation [1–3].
20 Not only does tropical forest Land-Use and Land-Cover Change (LULCC) constitute 10 to 15% of
21 the total global emissions [4], changes in forest fragmentation affect the forest structure and function.
22 Strong fragmentation effects decreases the number of large trees along forest edges [5,6], while species
23 composition and biodiversity are equally negatively affected [7–9]. Estimates show that 31% of carbon
24 emissions are caused by edge effects alone [10].

25 As such, anthropogenic factors through LULCC heavily affect forest structure and functioning
26 [10–12]. Accurate estimates of LULCC and forest canopy structure are therefore imperative to estimate
27 carbon emissions and other ecosystem services [1,2]. Remote sensing products have been key input as
28 they provide accurate spatial information to help estimate carbon emissions [1,13]. High resolution
29 aerial images provide scientists tools to monitor forest extent, structure and carbon emissions as canopy
30 texture is linked to above ground biomass [14–16]. Yet, these estimates are often limited in time to
31 recent decades [1,2,17,18].

32 Historical estimates of **Land-Use and Land-Cover (LULC)**, in the pre-satellite era (< 1972), exist
33 but generally rely on non-spatially explicit data (i.e socio-economic data) [2,17,19,20]. Efforts have
34 been made to use other geo-spatial data sources such as historical maps [21], declassified CORONA
35 satellite surveillance data across the US and central Brazil [22] as well as aerial surveys in post world
36 war II German [23]. Survey data across the African continent is less common, inaccessible or both.
37 Some studies do exist, as Buitenwerf *et al.* [24], Hudak and Wessman [25] and Okeke and Karnieli
38 [26] used aerial survey images to map vegetation changes in South African savannas and the Adulam
39 Nature Reserve, respectively, whilst Frankl *et al.* [27] and Nyssen *et al.* [28] mapped the Ethiopian
40 highlands of 1930's.

41 Despite the existence of large historical archives of aerial survey imagery for the central Congo
42 Basin (Figure 1, Appendix Figure 3) as of yet no studies have valorized these data. The lack of a
43 consistent valorization effort is unfortunate as the African rainforest is the second largest on Earth and
44 covers ~630 million ha, representing up to 66 Pg of carbon storage [29], and currently loses forest at an
45 increasing pace [30]. Given the impact of LULCC on the structure and functioning of central African
46 tropical forests, and their influence on both carbon dynamics [31] and biodiversity [9], accurate long
47 term reporting of historical forest cover warrants more attention [21].

48 Here, we use a combination of historical aerial photography and contemporary remote sensing
49 data to map long-term changes in the extent and structure of the tropical forest surrounding Yangambi,
50 in the central Congo Basin, effectively linking the start of the anthropocene [32] with current
51 assessments. Yangambi was, and remains, a focal center of forest and agricultural research and

52 development in the central Congo Basin. Past research in the region allows for thorough assessment of
53 land-use and land-cover change from a multi-disciplinary point of view, confronting us with complex
54 deforestation and land-use patterns.

55 We leverage Structure-from-Motion to generate a large orthomosaic of historical imagery and
56 develop a Convolutional Neural Network based forest cover mapping approach, based upon a
57 semi-supervised generated dataset extensively leveraging data augmentation. Our methodology
58 aims to provides a historical insight into important LULCC spatial patterns in Yangambi, such as
59 fragmentation and edge complexity. We further contextualize the influence of changes in the forest's life
60 history on past and current research into Above Ground Carbon (AGC) storage [31] and biodiversity
61 [9] in the central Congo Basin. Our fast scalable mapping approach for historical aerial survey data,
62 using limited supervised input, would further support long-term land-use and land-cover change
63 analysis across the central Congo Basin.

64 2. Methods

65 2.1. Historical data acquisition

66 Data for the central Congo Basin region, surrounding Kisangani, were collected in several flights
67 during the dry season of 1958 and 1959 (from 8/01/1958 to 20/02/1958 and from 28/12/1958 to
68 9/01/1959 respectively, see Appendix Figure 1) to generate topographic maps of the area, supervised
69 by the "Institut Géographique du Congo Belge" in Kinshasa (then Léopoldville). Black-and-White
70 infrared images (0.4 - 0.9 μm) were gathered along flight paths running mostly from west to east,
71 between **09:00 and 11:00** local time. Along a flight path continuous images were taken using a Wild
72 Heerburgg RC5a (currently Leica Geosystems) with an Aviogon lens assembly (114.83mm / f 5.6,
73 with a 90°view angle) resulting in square photo negative of 180 by 180 mm. Flights were flown at an
74 average absolute altitude of ~5200 m above sea level, covering roughly 18 530 km² at an approximate
75 scale of 1/40 000. The use of the integrated autograph system ensured timely acquisition of pictures
76 with a precise overlap (~1/3) between images. This large overlap between images together with flight
77 parameters would allow post-processing, using stereographs, to create accurate topographic maps.
78 Original data from this campaign are stored in the [Royal Museum for Central Africa](#) in Tervuren,
79 Belgium (Figure 1).

80 2.2. Site selection

81 We prioritised flight paths and images that contained current day permanent sampling plots,
82 larger protected areas, and past agricultural and forest research facilities (Figure 2). This selection
83 provides a comprehensive mapping of the Yangambi area and the life history of the forest surrounding

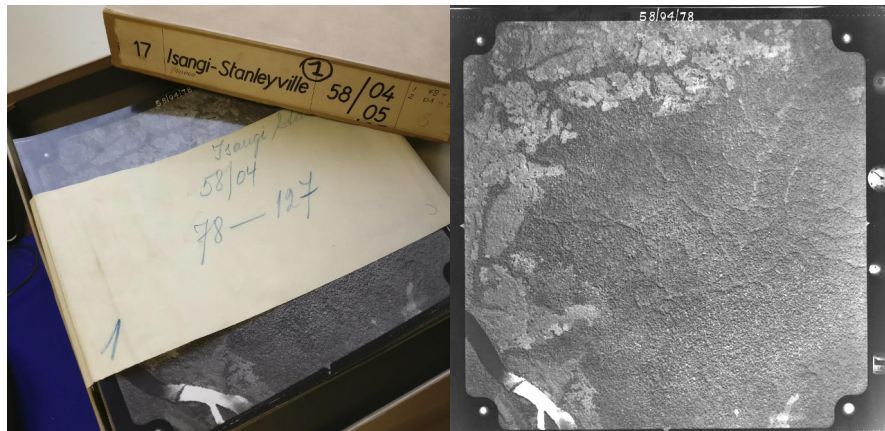


Figure 1. A box of historical aerial photographs (left) and a single aerial photograph (right) showing part of the Congo river. Note the meta-data provided in the margins of the image such as acquisition time and flight height and the solar glare on the Congo river.

84 it. Thereafter, we selected flight paths 1 through 11 for digitization. From this larger dataset of 334
 85 images we selected 74 survey images for orthomosaic compositing and further analysis. All the
 86 selected images stem from the flight campaign made during January and February of 1958. The area
 87 includes the Yangambi village, 20 contemporary permanent sampling plots [31], past and present
 88 agricultural experimental plots [33] and large sections of the Yangambi **UNESCO Man and Biosphere**
 89 **reserve** surrounding to the west and east of the village. Although not formally mosaicked we provided
 90 a full dataset of pre-processed images using the cropping and normalization routines described below.
 91 The latter data was not used in subsequent LULCC analysis, but has been archived and made available
 92 to the public separately (see code & data availability statement below).

93 2.3. Digitization and data processing

94 All selected images, covering the Yangambi area, were contact prints as original negatives of the
 95 prints were not available. Images were scanned at a resolution exceeding their original resolution
 96 (or grain) at the maximal physical resolution of an Epson A3 flatbed scanner (i.e. 2400 dpi or 160 MP
 97 per image) and saved as lossless tiff images. Data were normalized using contrast limited histogram
 98 equalization [34] with a window size of 32 and a clip limit of 1.5. Fiduciary marks were used to rectify
 99 and downsample the images into square 7700x7700 pixel images (~1200 dpi, 81 MP). This resulted in a
 100 dataset with digital images at a resolution that remained above the visible grain of the photographs,
 101 whilst the reduced image size facilitated easier file handling and processing speed.

102 Data was processed into a georeferenced orthomosaic using a Structure from motion (SfM, Ullman
 103 [35]) approach implemented in **Agisoft Metashape** version 1.5.2 (Agisoft LLC, St. Petersburg, Russia).
 104 An orthomosaic corrects remote sensing data to represent a perfectly downward looking image, free
 105 from perspective distortions due to topography and camera tilt. Using the SfM technique features,

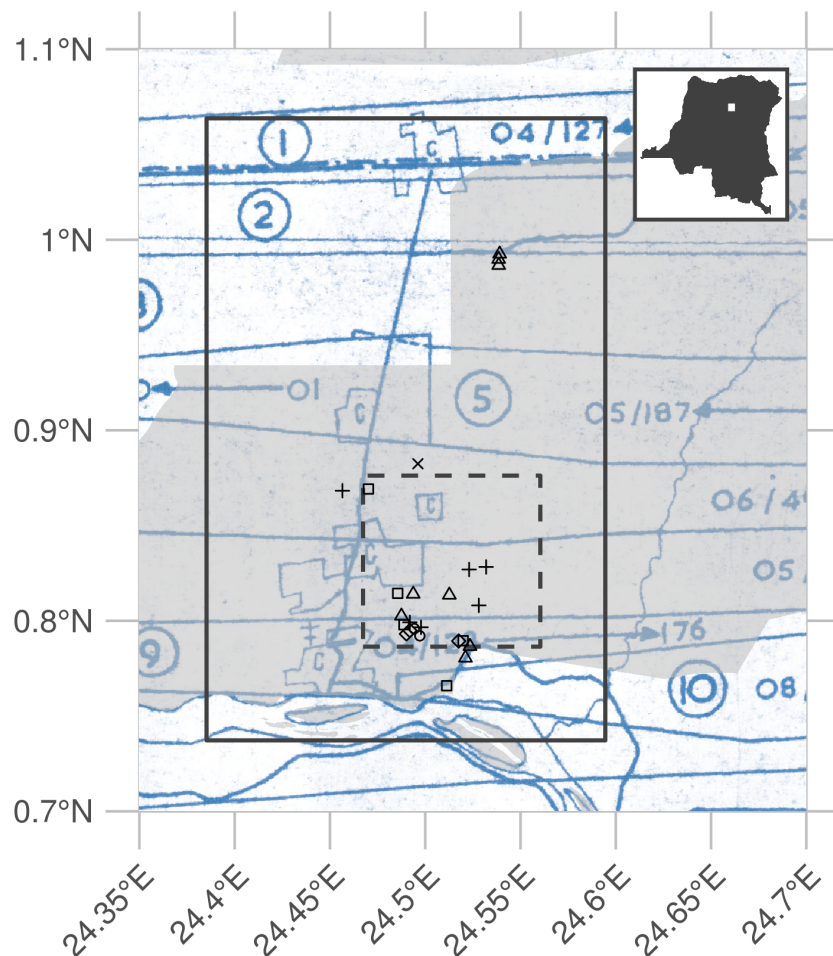


Figure 2. Overview of the historical flight paths during aerial photo acquisition and ancillary data used in this study. The bounding box of the orthomosaic data presented in this study is shown as a rectangle (23x36 km). The outline of a recent high-resolution Geo-eye panchromatic image is shown as a dashed dark grey rectangle (10x10km). The location of various permanent sampling plots are shown as x, +, and open squares and triangles for the mixed, mono-dominant and edge plots respectively. The grey polygon delineates the current day Yangambi Man and Biosphere reserve. The inset, top right, situates the greater Yangambi region (white rectangle) with the DR Congo. The full flight plan and details are shown in Appendix Figure 1 and 2

106 areas in images with a large degree of similarity, are matched across various images to reconstruct
107 a three dimensional scene (topography) from two-dimensional image sequences. During the SfM
108 analysis we masked clouds, glare or large water bodies such as the Congo river.

109 We calculated the orthomosaic using a low resolution point cloud and digital elevation map
110 (DEM). Additional ground control points were provided to assist in the referencing of image and
111 constrain the optimization routine used in the SfM algorithm. Ground control points consisted of
112 permanent structures which could be verified in both old and new aerial imagery (i.e. ESRI World
113 Imagery) and consisted of corner points of build structures (e.g. a building, bridge or swimming
114 pool etc.). Although clouds were removed during the SfM routine we did not mask all clouds in the
115 final orthomosaic to maximize forest coverage. The final scene was cropped, to provide consistent wall
116 to wall coverage of the reconstructed scene. The orthomosaic was exported as a geotiff for further
117 georeferencing in QGIS [36] using the georeferencer plugin (version 3.1.9) and additional ESRI World
118 Imagery high resolution reference data. We used 3rd degree polynomial and 16 ground control points
119 to correct the final image. Ground control points, raw image data and final processed image are
120 provided in addition to measures of uncertainty such as mean and median error across all ground
121 control points. All subsequent analysis are executed on the final geo-referenced orthomosaic or subsets
122 of it.

123 *2.4. Land-Use and Land-Cover Change*

124 *2.4.1. Classifying Land-Use and Land-Cover*

125 *Model training*

126 We automatically delineated all natural forest in the historical data, thus excluding tree plantations,
127 thinned or deteriorated forest stands which showed visible canopy cover loss, fields and buildings.
128 We used the Unet Convolutional Neural Net (CNN, Ronneberger *et al.* [37]) architecture implemented
129 in Keras [38] with an efficientnetb3 pre-processing backbone [39] running on TensorFlow [40] to train
130 a binary classifier (i.e. forest or non-forested). Training data were collected from the orthomosaic by
131 randomly selecting 513 pixel square tiles from locations within homogeneous forested or non-forested
132 polygons in the historical orthomosaic (Figure 5). Separate polygons were selected for training,
133 testing and validation purposes. Validation polygons were sampled 300 times, while both testing
134 and validation polygons were sampled at 100 random locations. Tiles extracted from locations
135 close to the polygon border at times contained mixed cover types. Tiles with mixed cover types
136 were removed from the list of source tiles (Table 1). Homogeneous source tiles were combined in
137 synthetic landscapes using a random gaussian field based binary mask (Figure 3). We generated 5000

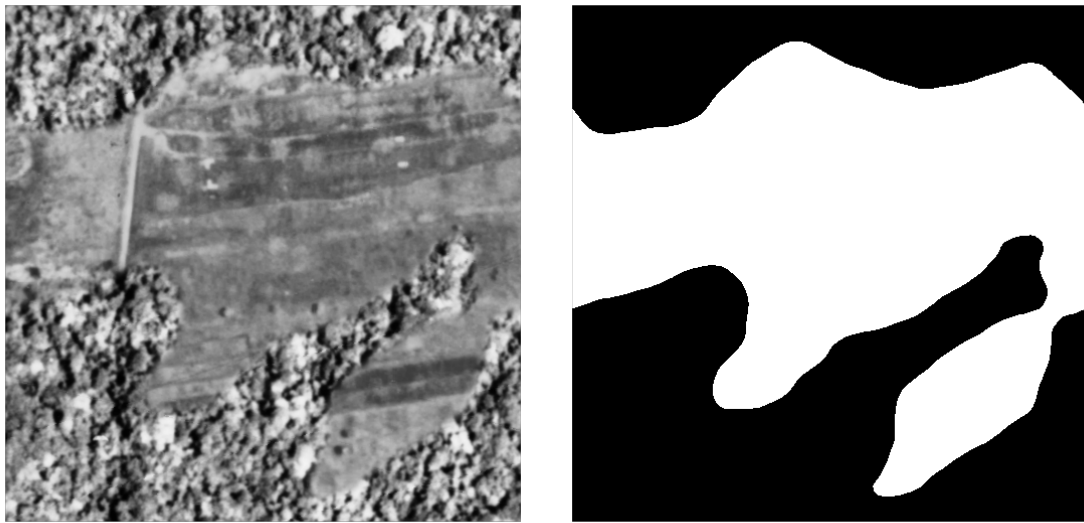


Figure 3. An example synthetic landscape, combining homogeneous forest and non-forest images into a patchy landscape using random gaussian field based masks. The left panel shows a combined synthetic landscape, while the right panel shows the corresponding forest (black) and non-forest (white) labels.

138 synthetic landscapes for training, while 500 landscapes were generated for both the validation and the
 139 testing datasets for a total of 6000 synthetic landscapes. In order to limit stitch line misclassifications,
 140 along the seams of mosaicked images, we created synthetic landscapes with different forest tiles
 141 to mimick forest texture transitions. We applied this technique to 10% of the generated synthetic
 142 landscapes (**across training, validation and testing data**).

Table 1. Number of source tiles used for the generation of synthetic landscapes.

	training	testing	validation
forest	300	100	100
non-forest	294	92	84

143 The CNN model was trained for 100 epochs with a batch size of 30 using Adam optimization [41],
 144 maximizing the Intersect-over-Union (IoU) using Sørensen–Dice and categorical cross-entropy loss
 145 functions. Data augmentation included random cropping to 320 pixel squares, random orientation,
 146 scaling, perspective, contrast and brightness shifts and image blurring. The optimized model was used
 147 to classify the complete orthomosaic using a moving window approach with a step size of 110 pixels
 148 and a majority vote (> 50% agreement) across overlapping areas to limit segmentation edge effects.
 149 **In addition we provide, raw pixel level classification agreement data for quality control purposes**
 150 **(see Data availability below)**. We refer to Figure 4 for a synoptic overview of the full deep learning
 151 learning workflow.

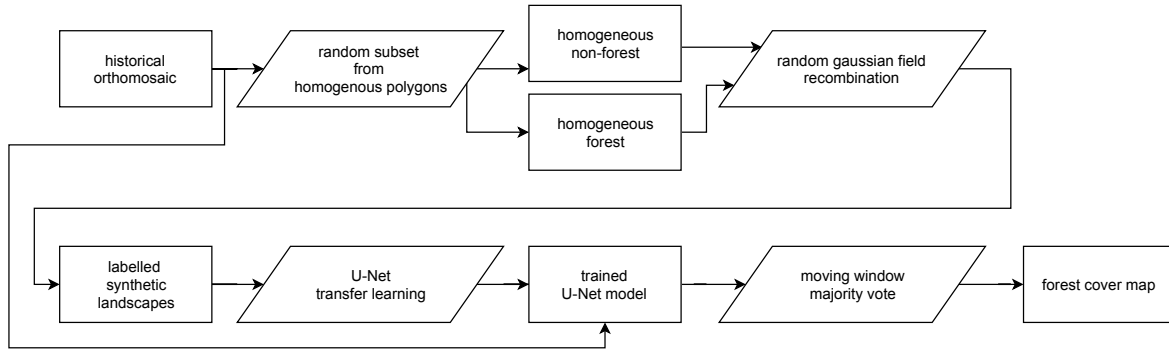


Figure 4. A diagram of the deep learning workflow followed in training a binary forest / non-forest cover convolutional neural net U-Net model to generate our forest cover map.

152 *Model validation*

153 We report the CNN accuracy based upon the IoU of our out-of-sample validation dataset
 154 of synthetic landscapes. In addition, we report confusion matrices for all pixels across the
 155 homogeneous validation polygons, as well as the training and testing polygons (see Figure
 156 5). Furthermore, we used the first acquisition of a recent pan-chromatic Geo-Eye 1 stereo pair
 157 (Geo-Eye, Thornton, Colorado, U.S.A., order 737537, 2011-11-11 08:55 GMT or 09:55 local time)
 158 to classify and assess the robustness of the CNN algorithm on contemporary remote sensing
 159 imagery with similar spectral and spatial characteristics. We used the Global Forest Change
 160 version 1.6 (GFC, tile 10N-020E) [1] map data, capturing forest loss up to 2011, to quantify accuracy
 161 on downsampled CNN Geo-Eye classification results. Once more, we report the confusion matrix
 162 of between the GFC and CNN derived forest cover maps, masking clouds and cloud shadows. To
 163 summarize confusion matrices we report accuracy as:

164
$$\text{Accuracy} = \frac{(TP+TN)}{(TP+TN+FP+FN)}$$

165 in which TP, TN, FP, FN are True Positive, True Negative, False Positive and False Negative,
 166 respectively.

167 2.4.2. Characterizing long term change

168 To map long term land-use and land-cover change in the Yangambi region we used the
 169 contemporary Global Forest Change version 1.6 (GFC, tile 10N-020E) map data [1]. Using the GFC
 170 data we calculated the latest state of the forest with respect to the conditions at the start of 1958, 60
 171 years earlier. In our analysis we only included GFC pixels which recorded no forest loss throughout
 172 the whole 2000 - 2018 period. As the resolution of the historical forest classification exceeds that of
 173 the GFC map we downsampled our historical forest cover data to 30m GFC resolution. We masked
 174 out all water bodies using the Global Forest Change survey data mask layer, and limited the analysis

175 to the right bank of the Congo river. Where the datasets overlap we provide summary statistics of
176 deforestation, reforestation and afforestation.

177 2.4.3. Landscape fragmentation & Above Ground Carbon estimates

178 To quantify changes in the structure of forest cover and its disturbances we used spatial pattern
179 analysis landscape fragmentation metrics [42]. We report the ratio of edge to area and the fractal
180 index to quantify landscape complexity of forest disturbances. Statistics were calculated for all forest
181 disturbance patches larger than 1 ha and smaller than the 95th percentile of the patch size distribution
182 using the R package landscapemetrics [43]. We provide mean and standard deviation on edge, area,
183 their ratio and fractal dimension for both the historical and contemporary Hansen *et al.* [1] forest cover
184 maps.

185 We estimated above ground carbon (AGC) losses and gains over time using plot based averages
186 of recent inventory data at permanent sampling plots in the area (Figure 2). We refer to Kearsley *et al.*
187 [31] for the survey method and allometric relations used to scale the survey data. Unlike standard
188 square 1 ha plots edge plots were set back 200m from forest edges and were 50x200m, with the 50m
189 side of the plot along the forest edge and continuing 200m into the forest (Appendix Table 1). We
190 further confirmed that forest edge plots did not show a significantly different AGC compared to those
191 of non-edged / mixed forest plots (Mann Whitney U test, $p < 0.05$). Thus it was not necessary to
192 explicitly quantify changes in AGC caused by edge effects. Moreover, we used the mean values of the
193 mixed forest as representative for potential AGC losses. Despite the challenges inherent in quantifying
194 AGC for forest edges we mapped the total extent of the edges in the contemporary landscape. To
195 align our landscape analysis with exploratory analysis of the survey data we used a buffer of 200m to
196 estimate the extent of forest edges and patches, up to the location of forest edge plots.

197 Surveys of old plantations show a large variation in AGC, depending on age and the crop type.
198 For example, the AGC values varied from 168.67 to 86.55 g Mg C ha⁻¹, for *Hevea brasiliensis* (rubber
199 tree) and *Elaeis guineensis* (oil palm) plots respectively (Bustillo *et al.* [44], personal communications).
200 These higher values are in line with the mixed AGC estimates in the area, while the palm plantations
201 resemble old-regrowth values (81.8 Mg C ha⁻¹, see **Appendix Table 1**). We therefore use both the
202 estimates of old-regrowth and mixed forest to estimate AGC for regrowth. We did not have sufficient
203 data to account for individual changes in AGC across plantations.

204 2.5. Canopy structure & FOTO texture analysis

205 We compared the structure of the canopy both visually and using Fourier Transform Textural
206 Ordination (FOTO, Couteron [45]). Fourier Transform Textural Ordination uses a principal component
207 analysis (PCA) on radially averaged 2D Fourier spectra to characterize canopy (image) texture. The

²⁰⁸ FOTO technique was first described by Couteron [45] to quantify canopy stucture in relation to biomass
²⁰⁹ and biodiversity, and can be used across multiple scenes using normalization [16].

²¹⁰ We used the standard FOTO methodology with fixed zones, instead of the moving window
²¹¹ approach. The window size was set to the same size (187 pixels or ~150 m) as used in the moving
²¹² window analysis above. To account for illumination differences between the two scenes we applied
²¹³ histogram matching. No global normalization was applied, as the scene was processed as a whole. PC
²¹⁴ values from this analysis for all permanent sampling plots in both image scences were extracted using
²¹⁵ a buffer with a radius of 50 m.

²¹⁶ For both site based and scene analysis we correlate PC values with permanent sample plot
²¹⁷ inventory data such as stem density, above ground biomass and tree species richness. Additional
²¹⁸ comparisons are made between contemporary Geo-Eye data and the historical orthomosaic derived PC
²¹⁹ values. Due to the few available permanent sampling plots in both scenes we used a non-parametric
²²⁰ paired signed rank (Wilcoxon) test to determine differences between the PC values of the Geo-Eye and
²²¹ historical orthomosaic image scenes across mono-dominant and mixed forest types. In all analysis,
²²² mono-dominant site 4 was removed from the analysis due to cloud contamination.

²²³ 3. Results

²²⁴ 3.1. Orthomosaic construction

²²⁵ Our analysis provides a first spatially explicity historical composite of aerial survey images **in**
²²⁶ **support of mapping land-use and land-cover** within the Congo Basin. The use of high resolution
²²⁷ historical images combined with structure from motion image processing techniques allowed us to
²²⁸ mosaic old imagery across a large extent. The final orthomosaic composition of the Yangambi region
²²⁹ **provided** an image scene covering approximately 733 million pixels across **~82800 ha** (~23x36 km,
²³⁰ Figure 2). The overall accuracy of the SfM orthomosaic composition was 0.88 m/pixel using the sparse
²³¹ cloud DEM for corrections at 45.8 m/pixel. The resulting georeferenced scene had a spatial accuracy
²³² of approximately **23 m**. Further georeferencing outside the SfM workflow reduced the mean error at
²³³ the ground control points to 5.3 ± 4.9 px ($\sim 4.7 \pm 4.3$ m), with a median error of 2.9 px (2.6 m). The
²³⁴ orthomosaic served as input for all subsequent LULCC analysis with all derived maps provided with
²³⁵ the manuscript repository (see data & code availability statements below).

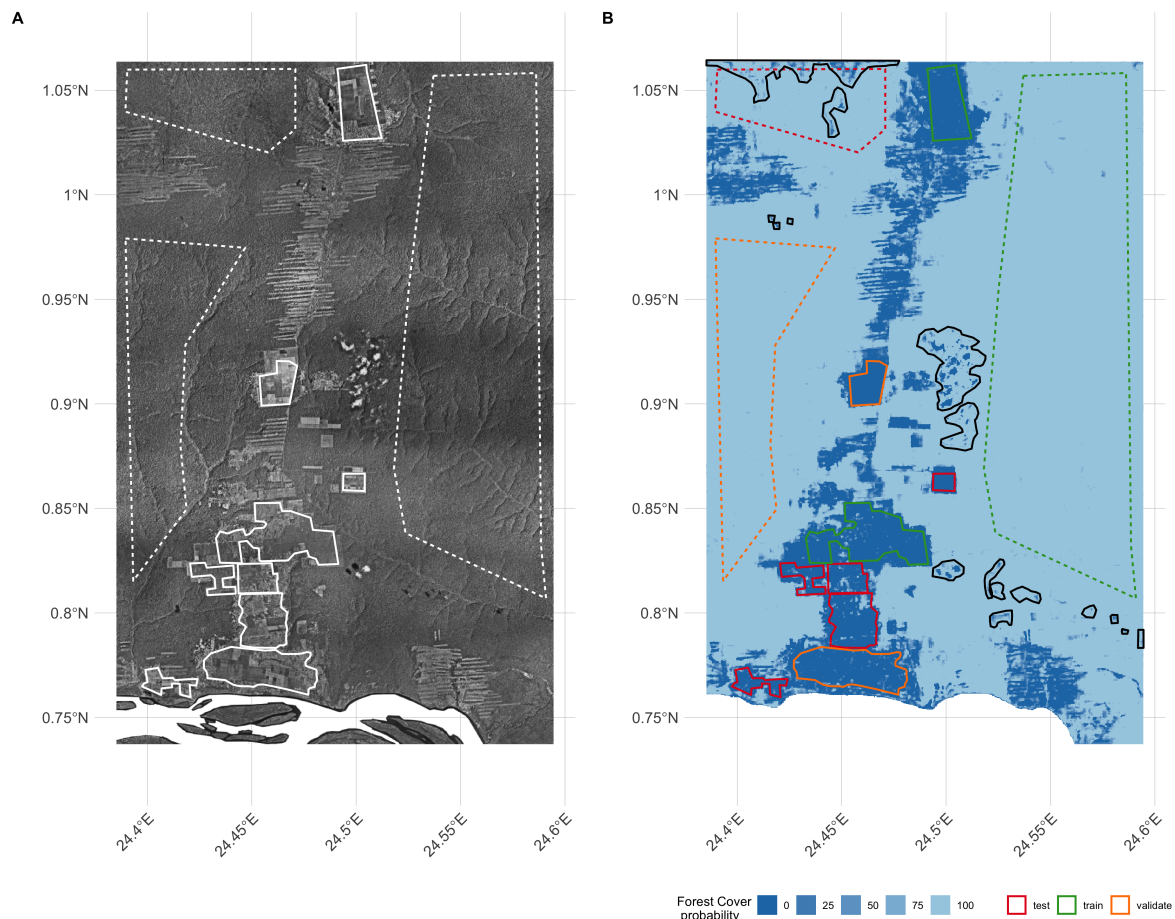


Figure 5. Overview of the final orthomosaic of the greater Yangambi region (A) as well as the forest cover classification uncertainty (B) used to generate the final Land Land Cover map (see Figure 6). Homogeneous polygons used in the generation of the synthetic landscape for Convolutional Neural Network training, testing and validation are marked as dashed and full lines for forest and non-forest regions, respectively. Training, testing and validation regions are denoted in panel B in green, red and orange, respectively. Black polygon outlines denote cloud and image stitch line regions which were manually excluded from analysis, but retained in calculation of validation statistics (see Table 2).

²³⁶ *3.2. Land-use and Land-Cover Classification*

²³⁷ *3.2.1. CNN model validation*

²³⁸ The CNN deep learning classifier reached an Intersection-over-Union (IoU) accuracy of 97%
²³⁹ on the detection of disturbed forest in the out-of-sample (validation) synthetic landscape data.
²⁴⁰ Using all pixels within the validation polygons (Figure 5) showed a similar accuracy value of
²⁴¹ ~98%. Using all polygons across the scene, including those used in the generation of testing and
²⁴² training synthetic landscapes, increased the accuracy to ~99% (Table 2). A comparison with recent
²⁴³ pan-chromatic Geo-Eye data shows good agreement, with an accuracy of ~87% across all pixels,
²⁴⁴ between the landsat based GFC data and downscaled CNN results (Table 2 and Figure 7).

Table 2. Confusion matrix showing % agreement between forest / non-forest classes using a Convolutional Neural Network (CNN) across previously selected homogenous areas.

CNN	Geo-Eye (full scene)		Aerial Survey (all polygons)		Aerial Survey (validation polygons)	
	non-forest	forest	non-forest	forest	non-forest	forest
non-forest	10.17	8.55	97.4	0.19	98.59	0.0
forest	3.75	77.52	2.6	99.81	1.41	100.0
Accuracy	87.70		98.61		99.3	

²⁴⁵ *3.3. Long term LULC changes and Above Ground Carbon*

²⁴⁶ Scaling our classifier to the whole historical orthomosaic we detected **16200 ha** (or ~20% of the
²⁴⁷ scene) of disturbed forests. A large fraction of the disturbed area was restored in the period between
²⁴⁸ the two acquisition periods. In total, **9900 ha**, or little over half of the affected forest was restored
²⁴⁹ (Figure 5C-D, dark blue). Recent deforested areas, as registered through satellite remote sensing,
²⁵⁰ approximate **8800 ha** (Table 3, Figure 6 - light green).

²⁵¹ Recent deforestation follows a distinctly different pattern compared to historical patterns.
²⁵² Historical deforestation showed a classical fishbone pattern for forest clearing with very sharp edges,
²⁵³ while current patterns are patchy and ad-hoc (figure 6C, dark blue and green colours respectively).
²⁵⁴ These differences are reflected in the analysis of landscape metrics of forest loss. Between the historical
²⁵⁵ and contemporary LULCC maps we see an increase in small disturbances, as indicated by the
²⁵⁶ decreasing area of the mean patch size, down to $\sim 1.86 \pm 0.75$ ha from $\sim 5.25 \pm 5.02$ ha historically.
²⁵⁷ Perimeter lengths were longer historically, at 1451 ± 943 m, compared to contemporary landscapes
²⁵⁸ $\sim 921 \pm 362$ m (Table 3). This shift in perimeter area ratio led to a similar change in the fractal index,
²⁵⁹ increasing in value to 1.1 ± 0.05 from 1.09 ± 0.04 over time. Values closer to a fractal index of 2 suggest
²⁶⁰ a more complex (fragmented) landscape.

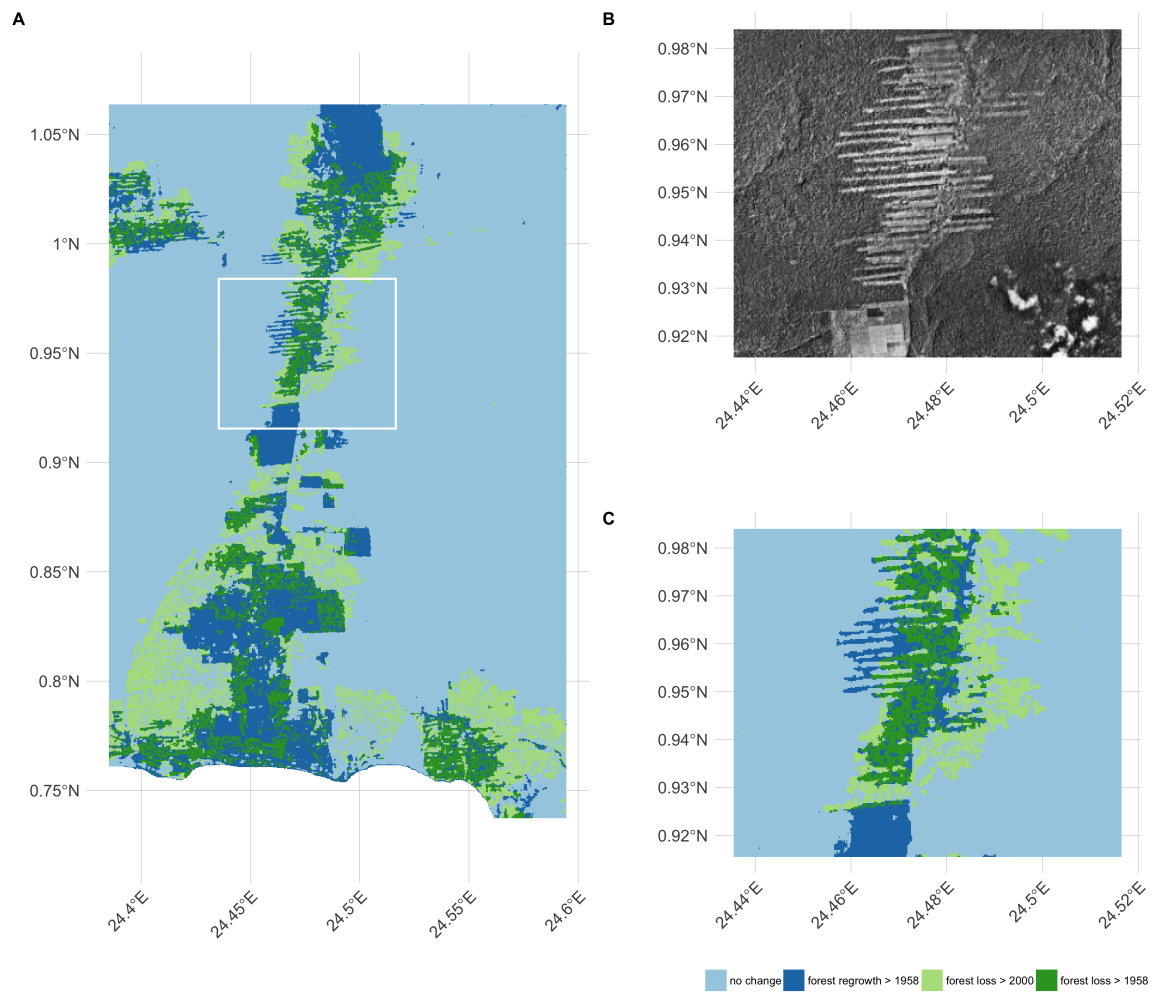


Figure 6. Overview of the final Land Use Land Cover Change map, a detailed inset of both the underlying orthomosaic (B) and the derived land use land cover change map displayed as the difference between the Convolutional Neural Network based classification orthomosaic and the recent Landsat based forest cover map by Hansen et al. 2013 (C).

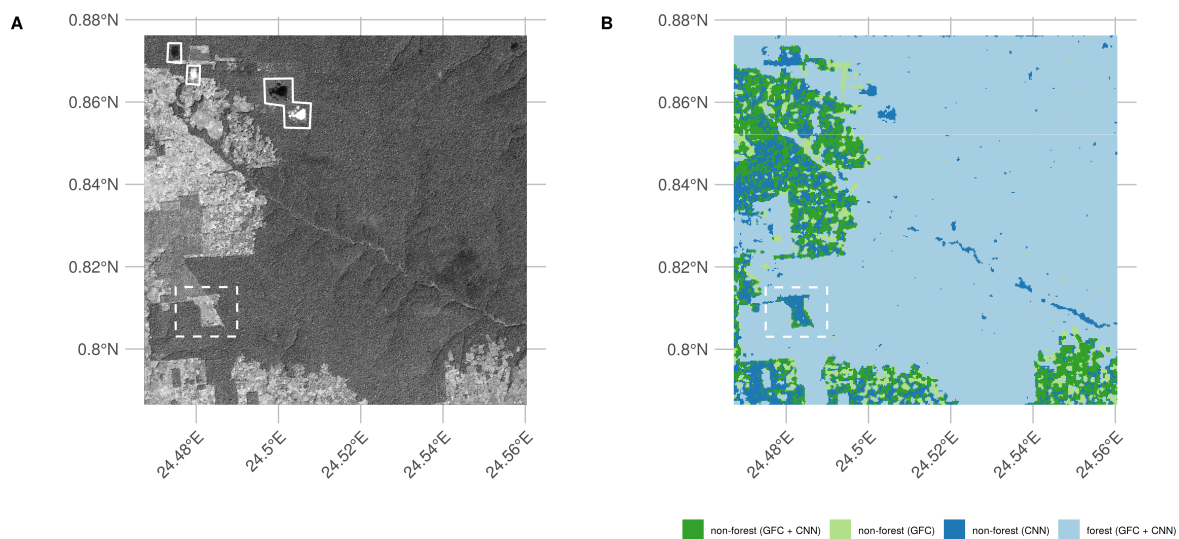


Figure 7. Convolutional Neural Network (CNN) based forest cover classification results (B) as run on a recent (2011) Geo-Eye panchromatic image (A). We show the difference between the Convolutional Neural Network based classification and a recent Landsat based forest cover map by Hansen et al. 2013. Full white outlines denote cloud contamination, the dashed rectangle shows a location where the CNN outperforms the Landsat based forest classification.

261 A comparison of forest edge plots with mixed forest plots showed no significant difference in
 262 AGC, or other reported values such as species richness, basal area or stem density (Mann Whitney U
 263 test, $p < 0.05$). Edge influence did not extend beyond 200 m from a forest edge, but still represented an
 264 area of **13200 ha**.

265 Changes in both land-use and land-cover led to concomitant changes in above ground carbon
 266 stocks. Recovery throughout the region was characterized for patches of forest and plantations.
 267 Assuming high density stands, based on previous work, this could amount to a carbon gains of 1592
 268 Gg C across our study area, offsetting more recent losses of approximately 1408 Gg C. On the other
 269 hand, at the low end, if we assume a lower carbon density of $81.8 \text{ Mg C ha}^{-1}$ this would result in a
 270 total carbon gain of 811 Gg C. Using our approach results indicate that overall deforestation around
 271 Yangambi has resulted in a loss of ~2416 Gg C in AGC stocks.

Table 3. Land use land cover change statistics of forest cover around Yangambi in the central Congo Basin. The data evaluates a difference between a historical (1958) aerial photography based survey and the Hansen et al. 2013 based satellite remote sensing data. Spatial coverage statistics are provided in square kilometers (km) and hectares (ha), rounded to the nearest integer as well as Above Ground Carbon (AGC) scaled using recent survey measurements.

	AGC	
	ha	(Gg C ha^{-1})
Forest	68455	
- of which edges	13151	
Regrowth > 1958 loss	9918	811 - 1592
Loss > 2000	8776	1408
Loss > 1958 (permanent)	6282	1008

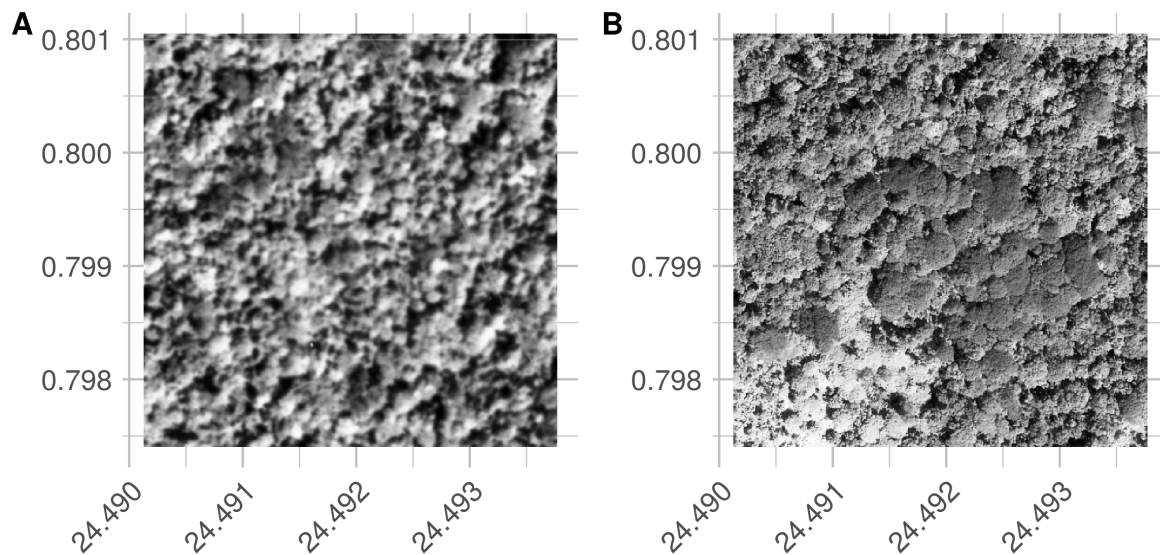


Figure 8. Visual comparison between a historical (A) and contemporary (B) permanent sampling plot. The site is currently listed as a mono-dominant *Brachystegia laurentii* stand. Note the structural differences with a 'coarse' canopy structure in the historical image compared to the more closed contemporary stand.

Table 4. Landscape metrics for historical and contemporary deforestation patterns. We report patch perimeter and area, their ratio and fractal dimension. Values are reported as mean \pm standard deviation, across all deforestation patches.

	perimeter (m)	area (ha)	ratio (m^{-1})	fractal dimension
historical	1451.58 ± 943.27	5.25 ± 5.02	0.03 ± 0.01	1.09 ± 0.04
contemporary	921.74 ± 362.59	1.86 ± 0.75	0.05 ± 0.01	1.1 ± 0.05

272 3.4. Canopy structure & FOTO texture analysis

273 Visual interpretation of the scenes provide evidence that most locations do not change dramatically
 274 with respect to canopy composition, except for the large areas of disturbances in contemporary fallow
 275 or young-regrowth plots. One marked difference is noted in the mono-dominant site 6 (Appendix
 276 Table 1). Here, the current mono-dominant *Brachystegia laurentii* is a recent development, changing the
 277 canopy structure visibly during the last half century (Figure 8). The previous varied canopy structure
 278 gave way to a more dense and uniform canopy. This is reflected in a change of the FOTO PC value from
 279 0.19 historically to its current value of 0.54. This historical value is similar to the mean of contemporary
 280 mono-dominant stands with PC averaging 0.34 ± 0.1 , and is only slightly higher than historical values
 281 for a mixed forest (0.18 ± 0.08). The reverse pattern is seen in the contemporary PC values. Here, the
 282 value of 0.54 exceeds those of most mono-dominant stands (0.35 ± 0.08), and is even further removed
 283 from the values noted for mixed forests (0.12 ± 0.03).

Using only small subsets around existing permanent sampling plots we show distinct differences between forest types, with PC values in both historical and contemporary imagery markedly higher for the mono-dominant forest types compared to all others (**Appendix Figure 4**). Provided that the young-regrowth and fallow permanent sampling plots have seen recent disturbance the Wilcoxon signed rank test on the mixed and mono-dominant plots between the historical and contemporary PC values did not show a significant difference ($p > 0.05$). Similarly, no significant different using PC values extracted from the whole scene analysis was noted ($p > 0.05$). Any relationships between contemporary Geo-Eye data and permanent sampling plot measurements of Above Ground Biomass, stem density and species richness were non-significant ($p > 0.05$, Appendix **Figures 5-7**).

Furthermore, visual inspection of the scene wide analysis suggests historical scenes do not show landscape wide canopy features (**Figure 9 A-B**), unlike the contemporary scene (**Figure 9 C-D**). Where the FOTO algorithm picks up landscape features such as changes in texture across the contemporary Geo-Eye scene (e.g. the river valley as a diagonal line in **Figure 9D**), however, no corresponding landscape patterns are found by the FOTO algorithm in the historical orthomosaic.

4. Discussion

Finely grained spatial data sources, such as remote sensing imagery, are rare before the satellite era (<1972). This lack of data limits our understanding of how forest structure has varied over longer time periods in remote areas. Long term assessment can be extended by using large inventories of historical aerial survey data [22,23,46]. Despite the difficulties in recovering this data and its limitations, such as invisible disturbances [47], remote sensing generally remains the best way to map and quantify LULCC [2]. In our study we used novel numerical remote sensing techniques to valorize, for the first time, historical remote sensing data in order to quantify (long term) land-use and land-cover change and canopy structural properties in the central Congo Basin. Despite these successes some methodological and research considerations remain.

4.1. Methodological considerations

4.1.1. Data recovery challenges

In our study the archive data recovered was limited to contact prints and therefore did not represent the true resolution of the original negative. In addition, analogue photography clearly produces a distinct softness compared to digital imagery (**Figure 8**). Despite favourable nadir image acquisitions [48] image softness combined with illumination effects between flight paths, and the self-similar nature of vast canopy expanses [49–51], limited our ability to provide wall-to-wall coverage of the entire dataset containing 334 images. Few man made features in the scenes also

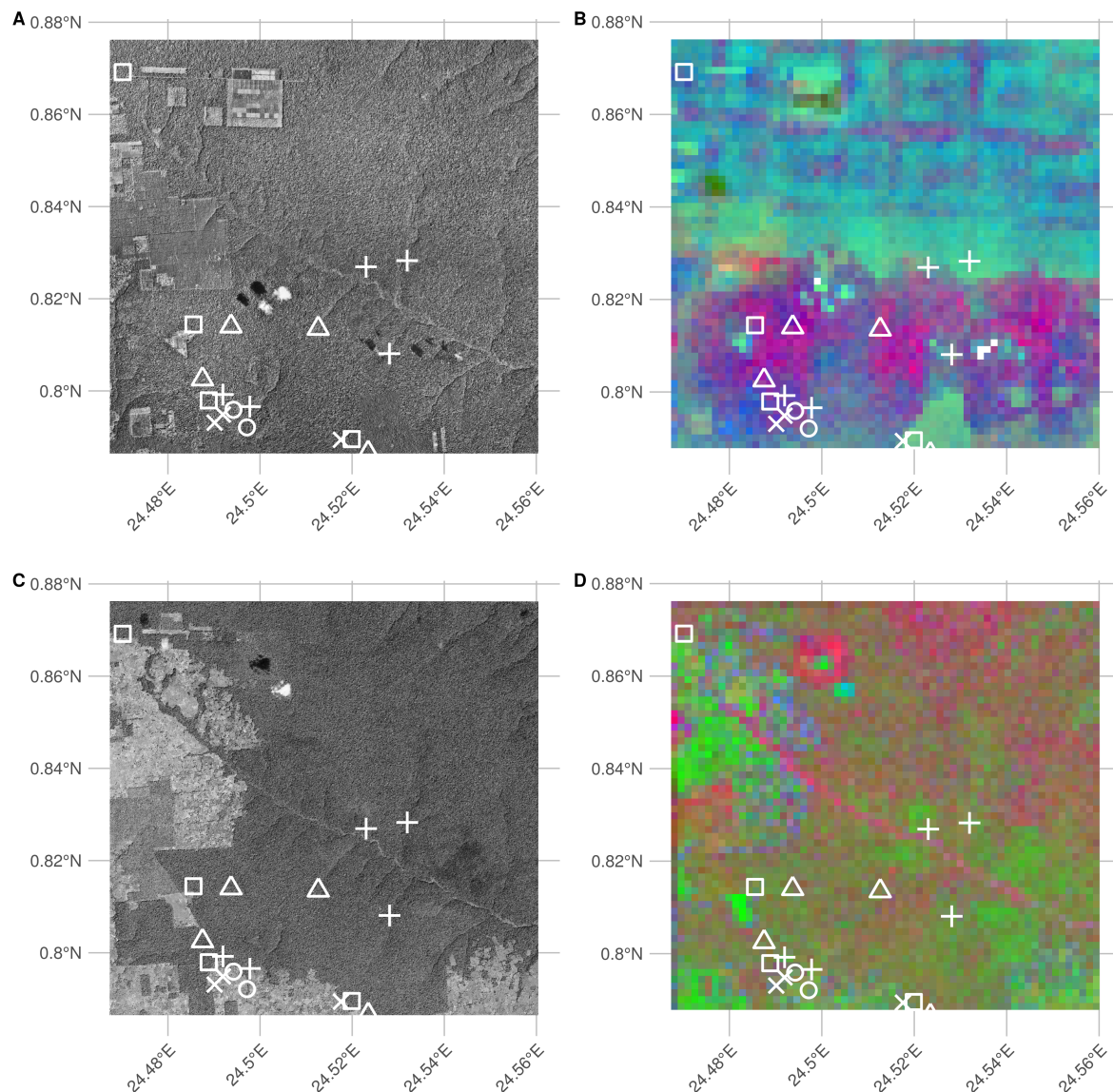


Figure 9. RGB visualizations of the first three principal components of scene wide FOTO texture analysis of historical and current (Geo-Eye) imagery. Current permanent sampling plots of mono-dominant, mixed, fallow and young (edge) forest plots are marked with open triangles, open circles, open squares and crosses, respectively.

316 made georeferencing challenging. Although the village of Yangambi provided a range of buildings
317 as (hard-edge) references, other areas within the central Congo Basin might have fewer permanent
318 structures and would require the use of soft-edged landscape features (e.g. trees, river outflows).
319 Research has shown that soft-edged features can help georeference scenes even when containing few
320 man-made features [52]. Our two step georeferencing approach resulted in a referencing accuracy of
321 $\sim 4.7 \pm 4.3$ m across reference points. However, it shoud be noted that referencing accuracy of the final
322 scene is less constrained toward the edges of the scene.

323 4.1.2. Land-use, Land-Cover change classification & validation

324 When classifying the orthomosaic into forest and non-forest states we favoured a deep
325 learning supervised classification using a CNN over manual segmentation to guarantee an
326 “apples-to-apples” comparison between the historical and the contemporary GFC forest cover map
327 used in our analysis. We acknowledge that both the CNN and GFC land-use and land-cover maps
328 use different underlying features, i.e. spatial or spectral data, yet attain a similarly high accuracy
329 of up to 99% [1]. More so, when validating our CNN classifier against GFC data (Figure 7) for a
330 contemporary high resolution Geo-Eye panchromatic image we reach an accuracy of $\sim 87\%$, despite
331 a time difference of almost 60 years. Visual inspection of the classification data in Figure 7 suggests
332 that the GFC map more often than not classifies non-forest areas as forest. Actual classification
333 accuracy of our algorithm might therefore be higher than our reported value.

334 4.1.3. Scaling opportunities

335 Our approach uses broadly defined homogeneous polygons to construct a balanced dataset
336 of synthethic landscapes. The methodology is analoguous to the use of sparse labelling as used
337 by [53] and contrasts with the standard methodologies which generally extract pixel (windows)
338 [22] or delineate land cover classes [23] to drive a classifier or analysis. More so, the use of heavy
339 image augmentation during model training sidesteps texture representation issues which affect
340 classification of image scenes with inconsistent illumination or sharpness [25] or ad-hoc feature
341 engineering [22]. The use of synthetic landscapes allowed us to account for most, but not all,
342 of the variability within our orthomosaic. More so, our analysis has shown that despite being
343 trained on historical data our model could map contemporary forest cover in remote sensing data
344 with similar spatial and spectral characteristics (Figure 7), suggesting that the classifier consistently
345 across works both space and time. We acknowledge that our approach will speed up labelling, but
346 is limited by the available homogeneous areas to sample from and the number of classes. Yet, the
347 latter should not be a constrained as previous research efforts have focussed on simple forest loss
348 maps [1].

349 4.2. Research context

350 4.3. Land-use, Land-Cover change & Above Ground Carbon

351 Our analysis shows that the majority of deforestation around Yangambi happened toward the late
352 1950's (**16200 ha**). Considerable regrowth has occurred since the aerial survey was executed (~**9900 ha**),
353 and socio-economic instability prevented further large scale forest exploitation. In particular, many
354 plantations have reached maturity and forest has re-established in previously cleared or disturbed
355 areas. The majority of this forest recovery takes the form of isolated patches of forest but is offset
356 by further deforestation of previously untouched forest. Generally, the function and structure of
357 forests can be influenced by forest edges that are located up to 1km away however most effects are
358 pronounced within the first 300m from the edge [54]. Our analysis of edge effects on AGC has shown
359 that the influence is negligible 200m away from the edge. Phillips *et al.* [55] have shown similar weak
360 responses to edge effects in the Amazon forest. Due to a lack of data on the extent (depth) of edge
361 effects and their influence on AGC beyond 200m we did not include any estimates of carbon loss
362 or gain within these zones. However, it must be stated that the influence of edges throughout the
363 landscape was not marginal. as these areas would account for **13200 ha**. Thus edges could have a
364 substantial negative [10] or positive [56] influence on AGC. Similarly, uncertainties in how to explicitly
365 correct for plantations in the landscape present a further challenge. Thus although our estimates
366 are only indicative they do underscore the important influence of landscape structure when carbon
367 accounting. However, our findings do not indicate that deforestation in Congo basin is declining, on
368 the contrary.

369 Over the past half century there has been a clear shift in land use in Yangambi (Figure 5). Land
370 use has shifted away from for example a regular fishbone deforestation pattern that emerges when
371 (large scale) agricultural interests dominate the landscape [57], to a more fragmented landscape
372 (Figure 5D). The latter former? is consistent with historical land management at the time of the aerial
373 survey [44]. These regular patterns have since been reversed because of a decrease in large scale
374 intensive agriculture, replaced by ad-hoc small scale subsistence farming with large perimeter to area
375 relationships (i.e. ragged edges). Consequently, edge effects in the current landscape are far more
376 pronounced than in the historical scene.

377 Visual inspection of the images also suggests that reforestation within the historically cleared areas
378 and experimental plots is not necessarily limited to areas far removed from more densely populated
379 areas. For example, large reforested areas exist close to the Congo stream and Yangambi village itself
380 (Fig. 5). Here, regional political components, such as land leases and large scale ownership could
381 have played a role in safeguarding some of these areas for rewinding or sustainable management

[58,59]. Despite widespread anthropogenic influences throughout the tropics [32] the retention of these forested areas show the potential of explicit or implicit protective policy measures (e.g. INERA concessions, Bustillo *et al.* [44]) on a multi-decadal time scale. Forest regrowth in non-continuous areas within Yangambi could increase landscape connectivity and help increase biodiversity [9].

Our analysis therefore provides an opportunity to highlight and study those regions that have previously suffered confirmed long-term disturbances, and those that have been restored since. Assessments of old plantations and recovering clear-cut forests can serve as a guide to help estimate carbon storage capacity and forest recovery rates in managed and unmanaged conditions [18,20,60] over the mid- to long-term, in support of rewilding and general forest restoration [9,58,59]. In addition, mapping long-term edge effects can further support research into issues such as receding forest edges [54].

4.4. Canopy structure & FOTO texture analysis

Finally, the FOTO technique used to quantify relationships between canopy structure and forest characteristics rendered no valuable insights of either the historical orthomosaic or recent Geo-Eye scene. Similarly weak correlations were found previously by Solórzano *et al.* [61]. In contrast, site based texture metric statistics did show correspondence between historical and contemporary satellite imagery. None of them were either consistent or significant. Although visual interpretation shows distinctly different canopy structures (Figure 5) the differences in how resolution is defined and issues related to image quality prevented us from quantifying these further. Unlike large scale studies by Ploton *et al.* [14] we could not scale this technique to historical data. **The successful use of our CNN classification model on a contemporary remote sensing data does suggest that texture can be used to consistently capture canopy properties 60 years apart. This suggests inflexibilit on part of the FOTO technique in dealing with non-standardized data.** We advise that future valorisation efforts should preferentially work from foto negatives (if available) to ensure optimal data quality in resolution, contrast and sharpness.

5. Conclusion

Given the impact of tropical forest disturbances on atmospheric CO₂ emissions, biodiversity and ecosystem productivity accurate long term reporting on land-cover and land-use change especially in the pre-satellite era is an imperative. Our analysis of historical aerial survey images of the Central Congo Basin provides a window into the state of the forest at the start of the anthropocene. Efforts to quantify canopy texture and their link to carbon storage had limited to no success. We have shown that historical aerial survey data can be used to quantify land-use and land-cover change using a highly automated workflow to quantify the structure and extent of forest cover change that can help assess the

415 impact of fragmentation on above ground carbon stocks. We also show a shift from previously highly
416 structured industrial deforestation of large areas **for plantation purposes**, to discrete smallholder
417 clearing for farming, increasing landscape fragmentation but also opportunity for substantial regrowth.
418 Efforts to quantify canopy texture and their link to carbon storage had limited to no success. As such,
419 our analysis provides insights into the state of rarely studied tropical forests and the rate at which
420 deforestation and reforestation has taken place over a multi-decadal scale in the central Congo basin
421 providing a useful historical context to land-cover and land-use change spatial patterns for interpreting
422 past and ongoing field research in the area.

423 6. Additional Information and Declarations

424 6.1. Data availability

425 Hufkens et al. (2019). A curated dataset of aerial survey images over the central Congo Basin,
426 1958. Zenodo: doi.org/10.5281/zenodo.3547767. All data not included in the latter repository can be
427 found bundled with the analysis code as listed below. Proprietary datasets (i.e. Geo-Eye data) are not
428 shared, but purchase order numbers allow for acquisition of these datasets to ensure reproducibility.

429 6.2. Code availability

430 All analysis code is available as an R / python [62] projects (<https://khufkens.github.io/orthodrc>
431 & https://khufkens.github.io/orthodrc_cnn/). The analysis relied heavily on the 'raster' [63],
432 'RStoolbox' [64], and 'landscapemetrics' [43] packages, while post-processing and plotting was
433 facilitated by the 'tidyverse' ecosystem [65], 'ggthemes' [66], 'scales' [67] and 'cowplot' [68]. Additional
434 plotting elements were formatted or provided by 'sf' [69] and 'rnaturalearth' [70] packages, respectively.
435 I'm grateful for the contributions to the scientific community by the developers of these packages.

436 **Acknowledgments:** This research was supported through the Belgian Science Policy office COBECORE
437 project (BELSPO; grant BR/175/A3/COBECORE). KH acknowledges funding from the European Union Marie
438 Skłodowska-Curie Action (project number 797668). I'm grateful for the support of Thales D'Haulleville
439 volunteering his time in scanning the images.

440 **Author Contributions:** K.H. conceived and designed the study, analyzed the data, prepared figures and tables,
441 authored, reviewed and approved the final draft of the manuscript. T.d.H. scanned all image data. E.K. and T.d.H.
442 provided plot based AGC estimates. T.D., K.J., E.K, H.B., P.S., F.V., S.M., M.A., J.V.D.B., H.V and L.W. reviewed the
443 final manuscript.

444 **Conflicts of Interest:** The authors declare no conflict of interest. The founding sponsors had no role in the design
445 of the study; in the collection, analyses, or interpretation of data; in the writing of the manuscript, and in the
446 decision to publish the results.

447 References

- 448 1. Hansen, M.C.; Potapov, P.V.; Moore, R.; Hancher, M.; Turubanova, S.A.; Tyukavina, A.; Thau, D.; Stehman,
449 S.V.; Goetz, S.J.; Loveland, T.R.; Kommareddy, A.; Egorov, A.; Chini, L.; Justice, C.O.; Townshend,
450 J.R.G. High-Resolution Global Maps of 21st-Century Forest Cover Change. *Science* **2013**, *342*, 850–853.
451 doi:10.1126/science.1244693.
- 452 2. Houghton, R.A.; House, J.I.; Pongratz, J.; van der Werf, G.R.; DeFries, R.S.; Hansen, M.C.; Le Quéré, C.;
453 Ramankutty, N. Carbon emissions from land use and land-cover change. *Biogeosciences* **2012**, *9*, 5125–5142.
454 doi:10.5194/bg-9-5125-2012.
- 455 3. Tyukavina, A.; Baccini, A.; Hansen, M.C.; Potapov, P.V.; Stehman, S.V.; Houghton, R.A.; Krylov, A.M.;
456 Turubanova, S.; Goetz, S.J. Aboveground carbon loss in natural and managed tropical forests from 2000 to
457 2012. *Environmental Research Letters* **2015**, *10*, 074002. doi:10.1088/1748-9326/10/7/074002.
- 458 4. van der Werf, G.R.; Morton, D.C.; DeFries, R.S.; Olivier, J.G.J.; Kasibhatla, P.S.; Jackson, R.B.; Collatz, G.J.;
459 Randerson, J.T. CO₂ emissions from forest loss. *Nature Geoscience* **2009**, *2*, 737–738. doi:10.1038/ngeo671.
- 460 5. Laurance, W.F.; Delamônica, P.; Laurance, S.G.; Vasconcelos, H.L.; Lovejoy, T.E. Rainforest fragmentation
461 kills big trees. *Nature* **2000**, *404*, 836–836. doi:10.1038/35009032.
- 462 6. Magnago, L.F.S.; Magrach, A.; Laurance, W.F.; Martins, S.V.; Meira-Neto, J.A.A.; Simonelli, M.; Edwards,
463 D.P. Would protecting tropical forest fragments provide carbon and biodiversity cobenefits under REDD+?
464 *Global Change Biology* **2015**, *21*, 3455–3468. doi:10.1111/gcb.12937.
- 465 7. Poorter, L.; Bongers, F. Leaf traits are good predictors of plant performance across 53 rain forest species.
466 *Ecology* **2006**, *87*, 1733–1743. doi:10.1890/0012-9658(2006)87[1733:LTAGPO]2.0.CO;2.
- 467 8. Barlow, J.; Lennox, G.D.; Ferreira, J.; Berenguer, E.; Lees, A.C.; Nally, R.M.; Thomson, J.R.; Ferraz, S.F.d.B.;
468 Louzada, J.; Oliveira, V.H.F.; Parry, L.; Ribeiro de Castro Solar, R.; Vieira, I.C.G.; Aragão, L.E.O.C.; Begotti,
469 R.A.; Braga, R.F.; Cardoso, T.M.; Jr, R.C.d.O.; Souza Jr, C.M.; Moura, N.G.; Nunes, S.S.; Siqueira, J.V.;
470 Pardini, R.; Silveira, J.M.; Vaz-de Mello, F.Z.; Veiga, R.C.S.; Venturieri, A.; Gardner, T.A. Anthropogenic
471 disturbance in tropical forests can double biodiversity loss from deforestation. *Nature* **2016**, *535*, 144–147.
472 doi:10.1038/nature18326.
- 473 9. Van de Perre, F.; Willig, M.R.; Presley, S.J.; Bapeamoni Andemwana, F.; Beeckman, H.; Boeckx, P.; Cooleman,
474 S.; de Haan, M.; De Kesel, A.; Dessein, S.; Grootaert, P.; Huygens, D.; Janssens, S.B.; Kearsley, E.; Kabeya,
475 P.M.; Leponce, M.; Van den Broeck, D.; Verbeeck, H.; Würsten, B.; Leirs, H.; Verheyen, E. Reconciling
476 biodiversity and carbon stock conservation in an Afrotropical forest landscape. *Science Advances* **2018**,
477 *4*, eaar6603. doi:10.1126/sciadv.aar6603.
- 478 10. Brinck, K.; Fischer, R.; Groeneveld, J.; Lehmann, S.; Dantas De Paula, M.; Pütz, S.; Sexton, J.O.; Song, D.;
479 Huth, A. High resolution analysis of tropical forest fragmentation and its impact on the global carbon
480 cycle. *Nature Communications* **2017**, *8*. doi:10.1038/ncomms14855.
- 481 11. Fauset, S.; Gloor, M.U.; Aidar, M.P.M.; Freitas, H.C.; Fyllas, N.M.; Marabesi, M.A.; Rochelle, A.L.C.;
482 Shenkin, A.; Vieira, S.A.; Joly, C.A. Tropical forest light regimes in a human-modified landscape. *Ecosphere*
483 **2017**, *8*, e02002. doi:10.1002/ecs2.2002.
- 484 12. Didham, R.K. Edge Structure Determines the Magnitude of Changes in Microclimate and Vegetation
485 Structure in Tropical Forest Fragments. *Biotropica* **1999**, *31*, 17–30.
- 486 13. Mitchard, E.T.A. The tropical forest carbon cycle and climate change. *Nature* **2018**, *559*, 527–534.
487 doi:10.1038/s41586-018-0300-2.
- 488 14. Ploton, P.; Pélassier, R.; Proisy, C.; Flavenot, T.; Barbier, N.; Rai, S.N.; Couturon, P. Assessing aboveground
489 tropical forest biomass using Google Earth canopy images. *Ecological Applications* **2012**, *22*, 993–1003.
- 490 15. Couturon, P.; Pelissier, R.; Nicolini, E.a.; Paget, D. Predicting tropical forest stand structure parameters
491 from Fourier transform of very high-resolution remotely sensed canopy images. *Journal of Applied Ecology*
492 **2005**, *42*, 1121–1128. doi:10.1111/j.1365-2664.2005.01097.x.
- 493 16. Barbier, N.; Couturon, P.; Proisy, C.; Malhi, Y.; Gastellu-Etchegorry, J.P. The variation of apparent crown
494 size and canopy heterogeneity across lowland Amazonian forests. *Global Ecology and Biogeography* **2010**,
495 *19*, 72–84. doi:10.1111/j.1466-8238.2009.00493.x.
- 496 17. DeFries, R.S.; Houghton, R.A.; Hansen, M.C.; Field, C.B.; Skole, D.; Townshend, J. Carbon emissions from
497 tropical deforestation and regrowth based on satellite observations for the 1980s and 1990s. *Proceedings of
498 the National Academy of Sciences* **2002**, *99*, 14256–14261. doi:10.1073/pnas.182560099.

- 499 18. Achard, F.; Beuchle, R.; Mayaux, P.; Stibig, H.J.; Bodart, C.; Brink, A.; Carboni, S.; Desclée, B.; Donnay, F.;
500 Eva, H.D.; Lüpi, A.; Rašić, R.; Seliger, R.; Simonetti, D. Determination of tropical deforestation rates and
501 related carbon losses from 1990 to 2010. *Global Change Biology* **2014**, *20*, 2540–2554. doi:10.1111/gcb.12605.
- 502 19. Ramankutty, N.; Foley, J.A. Estimating historical changes in global land cover: Croplands from 1700 to
503 1992. *Global Biogeochemical Cycles* **1999**, *13*, 997–1027. doi:10.1029/1999GB900046.
- 504 20. Sader, S.A.; Joyce, A.T. Deforestation Rates and Trends in Costa Rica, 1940 to 1983. *Biotropica* **1988**, *20*, 11.
505 doi:10.2307/2388421.
- 506 21. Willcock, S.; Phillips, O.L.; Platts, P.J.; Swetnam, R.D.; Balmford, A.; Burgess, N.D.; Ahrends, A.; Bayliss,
507 J.; Doggart, N.; Doody, K.; Fanning, E.; Green, J.M.H.; Hall, J.; Howell, K.L.; Lovett, J.C.; Marchant, R.;
508 Marshall, A.R.; Mbilinyi, B.; Munishi, P.K.T.; Owen, N.; Topp-Jorgensen, E.J.; Lewis, S.L. Land cover
509 change and carbon emissions over 100 years in an African biodiversity hotspot. *Global Change Biology* **2016**,
510 *22*, 2787–2800. doi:10.1111/gcb.13218.
- 511 22. Song, D.X.; Huang, C.; Sexton, J.O.; Channan, S.; Feng, M.; Townshend, J.R. Use of Landsat and
512 Corona data for mapping forest cover change from the mid-1960s to 2000s: Case studies from the Eastern
513 United States and Central Brazil. *ISPRS Journal of Photogrammetry and Remote Sensing* **2015**, *103*, 81–92.
514 doi:10.1016/j.isprsjprs.2014.09.005.
- 515 23. Nita, M.D.; Munteanu, C.; Gutman, G.; Abrudan, I.V.; Radloff, V.C. Widespread forest cutting in the
516 aftermath of World War II captured by broad-scale historical Corona spy satellite photography. *Remote
517 Sensing of Environment* **2018**, *204*, 322–332. doi:10.1016/j.rse.2017.10.021.
- 518 24. Buitenhof, R.; Bond, W.J.; Stevens, N.; Trollope, W.S.W. Increased tree densities in South African
519 savannas: >50 years of data suggests CO₂ as a driver. *Global Change Biology* **2012**, *18*, 675–684.
520 doi:10.1111/j.1365-2486.2011.02561.x.
- 521 25. Hudak, A.T.; Wessman, C.A. Textural Analysis of Historical Aerial Photography to Characterize Woody
522 Plant Encroachment in South African Savanna. *Remote Sensing of Environment* **1998**, *66*, 317–330.
523 doi:10.1016/S0034-4257(98)00078-9.
- 524 26. Okeke, F.; Karnieli, A. Methods for fuzzy classification and accuracy assessment of historical aerial
525 photographs for vegetation change analyses. Part I: Algorithm development. *International Journal of Remote
526 Sensing* **2006**, *27*, 153–176. doi:10.1080/01431160500166540.
- 527 27. Frankl, A.; Seghers, V.; Stal, C.; De Maeyer, P.; Petrie, G.; Nyssen, J. Using image-based modelling
528 (SfM-MVS) to produce a 1935 ortho-mosaic of the Ethiopian highlands. *International Journal of Digital Earth*
529 **2015**, *8*, 421–430. doi:10.1080/17538947.2014.942715.
- 530 28. Nyssen, J.; Petrie, G.; Mohamed, S.; Gebremeskel, G.; Seghers, V.; Debever, M.; Hadgu, K.M.; Stal, C.; Billi,
531 P.; Demaeyer, P.; Haile, M.; Frankl, A. Recovery of the aerial photographs of Ethiopia in the 1930s. *Journal
532 of Cultural Heritage* **2016**, *17*, 170–178. doi:10.1016/j.culher.2015.07.010.
- 533 29. Lewis, S.L.; Lopez-Gonzalez, G.; Sonké, B.; Affum-Baffoe, K.; Baker, T.R.; Ojo, L.O.; Phillips, O.L.; Reitsma,
534 J.M.; White, L.; Comiskey, J.A.; Djuiukouo K, M.N.; Ewango, C.E.N.; Feldpausch, T.R.; Hamilton, A.C.;
535 Gloor, M.; Hart, T.; Hladik, A.; Lloyd, J.; Lovett, J.C.; Makana, J.R.; Malhi, Y.; Mbago, F.M.; Ndangalasi,
536 H.J.; Peacock, J.; Peh, K.S.H.; Sheil, D.; Sunderland, T.; Swaine, M.D.; Taplin, J.; Taylor, D.; Thomas, S.C.;
537 Votere, R.; Wöll, H. Increasing carbon storage in intact African tropical forests. *Nature* **2009**, *457*, 1003–1006.
538 Publisher: Earth and Biosphere Institute, School of Geography, University of Leeds, Leeds LS2 9JT, UK.
539 s.l.lewis@leeds.ac.uk.
- 540 30. Butsic, V.; Baumann, M.; Shortland, A.; Walker, S.; Kuemmerle, T. Conservation and conflict in the
541 Democratic Republic of Congo: The impacts of warfare, mining, and protected areas on deforestation.
542 *Biological Conservation* **2015**, *191*, 266–273. doi:10.1016/j.biocon.2015.06.037.
- 543 31. Kearsley, E.; de Haulleville, T.; Hufkens, K.; Kidimbu, A.; Toirambe, B.; Baert, G.; Huygens, D.; Kebede,
544 Y.; Defourny, P.; Bogaert, J.; Beeckman, H.; Steppe, K.; Boeckx, P.; Verbeeck, H. Conventional tree
545 height-diameter relationships significantly overestimate aboveground carbon stocks in the Central Congo
546 Basin. *Nature communications* **2013**, *4*, 2269. doi:10.1038/ncomms3269.
- 547 32. Lewis, S.L.; Maslin, M.A. Defining the Anthropocene. *Nature* **2015**, *519*, 171–180. doi:10.1038/nature14258.
- 548 33. Bauters, M.; Ampoorter, E.; Huygens, D.; Kearsley, E.; De Haulleville, T.; Sellan, G.; Verbeeck, H.; Boeckx,
549 P.; Verheyen, K. Functional identity explains carbon sequestration in a 77-year-old experimental tropical
550 plantation. *Ecosphere* **2015**, *6*, art198. doi:10.1890/ES15-00342.1.

- 551 34. Zuiderveld, K. Contrast Limited Adaptive Histogram Equalization. In *Graphics GEMs IV*; Academic Press:
552 San Diego, CA, USA, 1994; pp. 474–485.
- 553 35. Ullman, S. The Interpretation of Structure from Motion. *Proceedings of the Royal Society of London. Series B, Biological Sciences* **1979**, *203*, 405–426.
- 554 36. QGIS Development team., QGIS Geographic Information System., 2018. Available at: <http://qgis.osgeo.org>.
- 555 37. Ronneberger, O.; Fischer, P.; Brox, T. U-Net: Convolutional Networks for Biomedical Image Segmentation.
556 In *Medical Image Computing and Computer-Assisted Intervention – MICCAI 2015*; Navab, N.; Hornegger, J.;
557 Wells, W.M.; Frangi, A.F., Eds.; Springer International Publishing: Cham, 2015; Vol. 9351, pp. 234–241.
558 doi:10.1007/978-3-319-24574-4_28.
- 559 38. Chollet, F. Keras, 2015. Available at: <https://github.com/fchollet/keras>.
- 560 39. Yakubovskiy, P. Segmentation Models, 2019. Available at: https://github.com/qubvel/segmentation_models.
- 561 40. Martín Abadi.; Ashish Agarwal.; Paul Barham.; Eugene Brevdo.; Zhifeng Chen.; Craig Citro.; Greg S.
562 Corrado.; Andy Davis.; Jeffrey Dean.; Matthieu Devin.; Sanjay Ghemawat.; Ian Goodfellow.; Andrew
563 Harp.; Geoffrey Irving.; Michael Isard.; Jia, Y.; Rafal Jozefowicz.; Lukasz Kaiser.; Manjunath Kudlur.; Josh
564 Levenberg.; Dandelion Mané.; Rajat Monga.; Sherry Moore.; Derek Murray.; Chris Olah.; Mike Schuster.;
565 Jonathon Shlens.; Benoit Steiner.; Ilya Sutskever.; Kunal Talwar.; Paul Tucker.; Vincent Vanhoucke.; Vijay
566 Vasudevan.; Fernanda Viégas.; Oriol Vinyals.; Pete Warden.; Martin Wattenberg.; Martin Wicke.; Yuan Yu.;
567 Xiaoqiang Zheng. TensorFlow: Large-Scale Machine Learning on Heterogeneous Systems, 2015. Available
568 at: <https://www.tensorflow.org/>.
- 569 41. Kingma, D.P.; Ba, J. Adam: A Method for Stochastic Optimization. *arXiv:1412.6980 [cs]* **2017**. arXiv:
570 1412.6980.
- 571 42. Dale, M.R.T. *Spatial pattern analysis in plant ecology*; Cambridge studies in ecology, Cambridge University
572 Press: Cambridge ; New York, 1999.
- 573 43. Hesselbarth, M.H.K.; Sciaiani, M.; With, K.A.; Wiegand, K.; Nowosad, J. landscapemetrics: an open-source
574 R tool to calculate landscape metrics. *Ecography* **2019**.
- 575 44. Bustillo, E.; Raets, L.; Beeckman, H.; Bourland, N.; Rousseau, M.; Hubau, W.; De Mil, T. Evaluation du
576 potentiel énergétique de la biomasse aérienne ligneuse des anciennes plantations de l'INERA Yangambi.
577 Technical report, CIFOR, 2018.
- 578 45. Couteron, P. Quantifying change in patterned semi-arid vegetation by Fourier analysis of digitized aerial
579 photographs. *International Journal of Remote Sensing* **2002**, *23*, 3407–3425. doi:10.1080/01431160110107699.
- 580 46. Kadmon, R.; Harari-Kremer, R. Studying Long-Term Vegetation Dynamics Using Digital
581 Processing of Historical Aerial Photographs. *Remote Sensing of Environment* **1999**, *68*, 164–176.
582 doi:10.1016/S0034-4257(98)00109-6.
- 583 47. Peres, C.A.; Barlow, J.; Laurance, W.F. Detecting anthropogenic disturbance in tropical forests. *Trends in
584 Ecology & Evolution* **2006**, *21*, 227–229. doi:10.1016/j.tree.2006.03.007.
- 585 48. Verhoeven, G. BRDF and its Impact on Aerial Archaeological Photography: BRDF and its impact on aerial
586 archaeological photography. *Archaeological Prospection* **2017**, *24*, 133–140. doi:10.1002/arp.1559.
- 587 49. Park, J.Y.; Muller-Landau, H.C.; Lichstein, J.W.; Rifai, S.W.; Dandois, J.P.; Bohlman, S.A. Quantifying Leaf
588 Phenology of Individual Trees and Species in a Tropical Forest Using Unmanned Aerial Vehicle (UAV)
589 Images. *Remote Sensing* **2019**, *11*, 1534. doi:10.3390/rs11131534.
- 590 50. Simini, F.; Anfodillo, T.; Carrer, M.; Banavar, J.R.; Maritan, A. Self-similarity and scaling
591 in forest communities. *Proceedings of the National Academy of Sciences* **2010**, *107*, 7658–7662.
592 doi:10.1073/pnas.1000137107.
- 593 51. Sole, R.V.; Manrubia, S.C. Self-similarity in rain forests: evidence for a critical state. *Physical Review E* **1995**,
594 *51*, 6250 – 6253.
- 595 52. Hughes, M.L.; McDowell, P.F.; Marcus, W.A. Accuracy assessment of georectified aerial photographs:
596 Implications for measuring lateral channel movement in a GIS. *Geomorphology* **2006**, *74*, 1–16.
597 doi:10.1016/j.geomorph.2005.07.001.
- 598 53. Buscombe, D.; Ritchie, A. Landscape Classification with Deep Neural Networks. *Geosciences* **2018**, *8*, 244.
599 doi:10.3390/geosciences8070244.

- 603 54. Gascon, C.; Williamson, G.B.; Fonseca, G.A.B.d. Receding Forest Edges and Vanishing Reserves. *Science, New Series* **2000**, *288*, 1356–1358.
- 604 55. Phillips, O.L.; Rose, S.; Mendoza, A.M.; Vargas, P.N. Resilience of Southwestern Amazon Forests to Anthropogenic Edge Effects. *Conservation Biology* **2006**, *20*, 1698–1710. doi:10.1111/j.1523-1739.2006.00523.x.
- 605 56. Reinmann, A.B.; Hutyra, L.R. Edge effects enhance carbon uptake and its vulnerability to climate change in temperate broadleaf forests. *Proceedings of the National Academy of Sciences* **2017**, *114*, 107–112. doi:10.1073/pnas.1612369114.
- 606 57. Arima, E.Y.; Walker, R.T.; Perz, S.; Souza, C. Explaining the fragmentation in the Brazilian Amazonian forest. *Journal of Land Use Science* **2015**, pp. 1–21. doi:10.1080/1747423X.2015.1027797.
- 607 58. Arima, E.Y.; Barreto, P.; Araújo, E.; Soares-Filho, B. Public policies can reduce tropical deforestation: Lessons and challenges from Brazil. *Land Use Policy* **2014**, *41*, 465–473. doi:10.1016/j.landusepol.2014.06.026.
- 608 59. Larson, A.M. Forest tenure reform in the age of climate change: Lessons for REDD+. *Global Environmental Change* **2011**, *21*, 540–549. doi:10.1016/j.gloenvcha.2010.11.008.
- 609 60. Gourlet-Fleury, S.; Mortier, F.; Fayolle, A.; Baya, F.; Ouédraogo, D.; Bénédict, F.; Picard, N. Tropical forest recovery from logging: a 24 year silvicultural experiment from Central Africa. *Philosophical Transactions of the Royal Society B: Biological Sciences* **2013**, *368*, 20120302. doi:10.1098/rstb.2012.0302.
- 610 61. Solórzano, J.V.; Gallardo-cruz, J.A.; González, E.J.; Peralta-carreta, C.; Hernández-gómez, M.; Oca, A.F.m.D.; Cervantes-jiménez, L.G.; Solórzano, J.V.; Gallardo-cruz, J.A.; González, E.J.; Peralta-carreta, C.; Hernández-gómez, M.; Oca, A.F.m.D.; Cervantes-jiménez, L.G. Contrasting the potential of Fourier transformed ordination and gray level co-occurrence matrix textures to model a tropical swamp forest 's structural and diversity attributes. *Journal of Applied Remote Sensing* **2018**, *12*, 036006. doi:10.1111/1.JRS.12.036006.
- 611 62. R Core Team. *R: A Language and Environment for Statistical Computing*; R Foundation for Statistical Computing: Vienna, Austria, 2019.
- 612 63. Hijmans, R.J. raster: Geographic Data Analysis and Modeling, 2019. Available at: <https://CRAN.R-project.org/package=raster>.
- 613 64. Leutner, B.; Horning, N.; Schwalb-Willmann, J. RStoolbox: Tools for Remote Sensing Data Analysis, 2019. Available at: <https://CRAN.R-project.org/package=RStoolbox>.
- 614 65. Wickham, H. tidyverse: Easily Install and Load the 'Tidyverse', 2017. Available at: <https://CRAN.R-project.org/package=tidyverse>.
- 615 66. Arnold, J.B. ggthemes: Extra Themes, Scales and Geoms for 'ggplot2', 2019. Available at: <https://CRAN.R-project.org/package=ggthemes>.
- 616 67. Wickham, H. scales: Scale Functions for Visualization, 2018. Available at: <https://CRAN.R-project.org/package=scales>.
- 617 68. Wilke, C.O. cowplot: Streamlined Plot Theme and Plot Annotations for 'ggplot2', 2019. Available at: <https://CRAN.R-project.org/package=cowplot>.
- 618 69. Pebesma, E. Simple Features for R: Standardized Support for Spatial Vector Data. *The R Journal* **2018**, *10*, 439–446. doi:10.32614/RJ-2018-009.
- 619 70. South, A. rnaturalearth: World Map Data from Natural Earth, 2017. Available at: <https://CRAN.R-project.org/package=rnaturalearth>.